Electronic Supplemental Information for:

Observation of Low Temperature n-p Transition in Individual Titania Nanotubes

Hatem Brahmi,[a] Ram Neupane,[b] Lixin Xie,[b] Shivkant Singh,[ac] Milad Yarali,[a] Giwan Katwal,[b] Shuo Chen,[b] Maggie Paulose,[b] Oomman K. Varghese*[b] and Anastassios Mavrokefalos*[a]

[a]Department of Mechanical Engineering, University of Houston, Houston, TX 77204, USA. E-mail: amavrokefalos@uh.edu

[b]Department of Physics, University of Houston, Houston, TX 77204, USA. E-mail: okvarghese@uh.edu

[c]Material Science and Engineering Program, University of Houston, Houston, TX 77204, USA

Transmission Electron Microscopy

High resolution transmission electron microscopy (HRTEM) study was done using JEOL 2000-SFX microscope. The results from the actual nanotubes used for thermal and electrical measurements are shown in Figure 1. Additionally, we tried to find whether there was a distinct change in the grain dimensions after lattice reduction. For this study, we used nanotubes prepared under identical conditions as NT1 (reduced) and NT4 (unreduced). Nevertheless, moire patterns formed by overlapping grains made the task difficult [see Figure S1 (a,b)]. Furthermore, the grain boundaries were not easily distinguishable [see Figure S1 (c,d)]. The grain size was determined to be in the range of a few tens of nanometers in both the samples. Although a

detailed investigation was done by taking lattice images at different regions of nanotubes from both sample types, no evidences showing the influence of forming gas annealing on grain size was found. This was not unexpected as both the samples were annealed first at 530 °C and the sample for lattice reduction (NT1) was subjected to annealing at a lower temperature (500 °C).

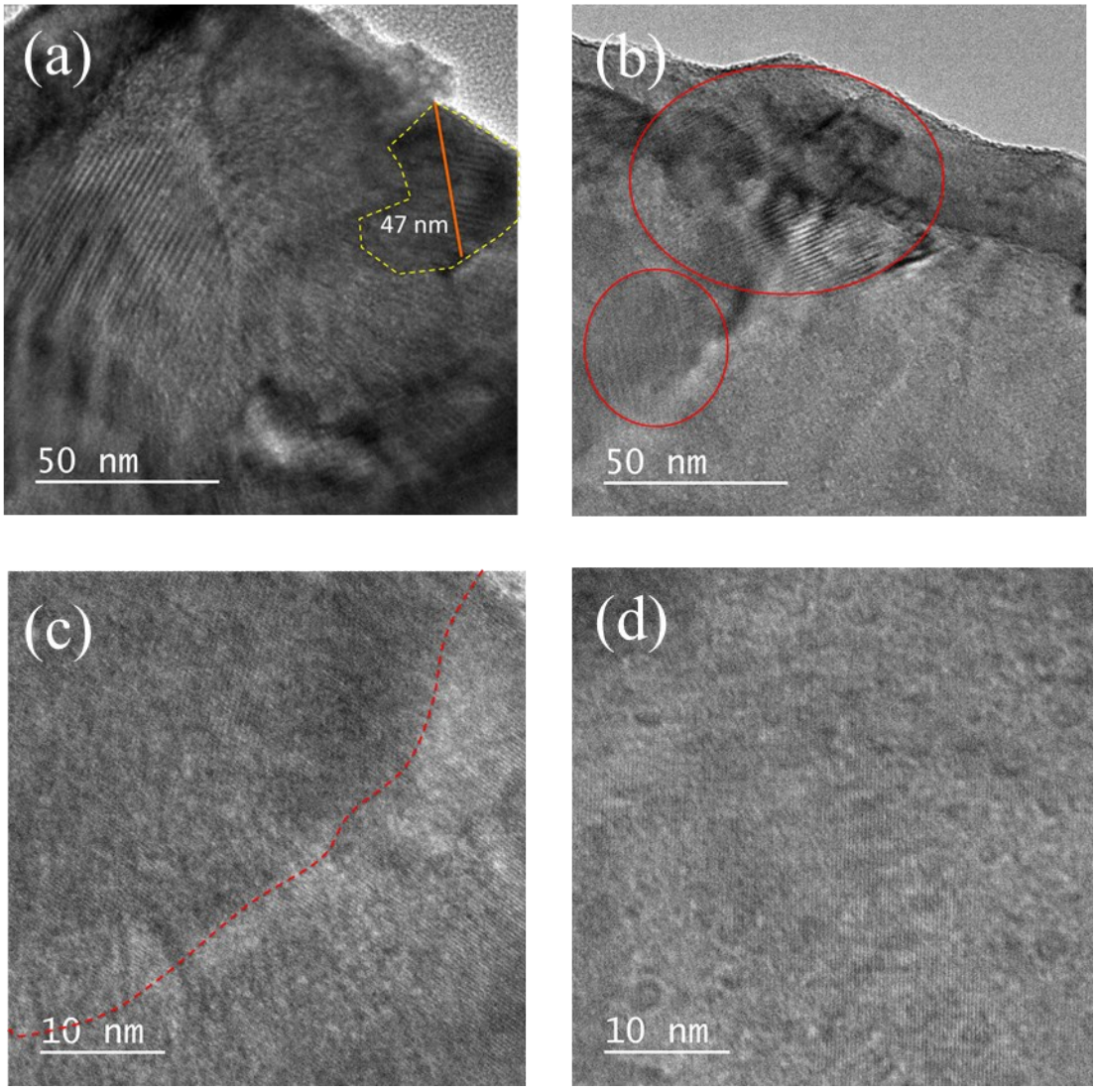

Fig. S1. HRTEM images from a nanotube in the class NT1 (a, c) and NT4 (b, d). The dashed curve in (c) shows a region that is possibly a grain boundary.

Thermal conductivity modeling

Callaway model developed by Morelli *et al.*[1] was used to interpolate the phonon scattering rates to the measured thermal conductivity. The model suggests the contribution of both longitudinal and acoustic modes independently. Phonon group velocity and Debye temperature are deduced from the bulk phonon dispersion curves. The thermal conductivity is written as:

$$\kappa = \kappa_L + 2\kappa_T \tag{1}$$

where κ_L and κ_T are the longitudinal transverse phonon branch contributions respectively. And for each branch:

$$\kappa_{L(T)} = \kappa_{L1(T1)} + \kappa_{L2(T2)} \tag{2}$$

Where the partial thermal conductivities are:

$$\kappa_{i1} = \frac{1}{3} C_i T^3 \int_0^{\theta_i/T} \frac{\tau_C^i(x) x^4 e^x}{(e^x - 1)^2} dx \tag{3}$$

$$\kappa_{i2} = \frac{1}{3} C_i T^3 \frac{\left[\int_0^{\theta_i/T} \frac{\tau_C^i(x) x^4 e^x}{\tau_N^i(x)(e^x - 1)^2} dx\right]^2}{\int_0^{\theta_i/T} \frac{\tau_C^i(x) x^4 e^x}{\tau_N^i(x)\tau_R^i(x)(e^x - 1)^2} dx} \tag{4}$$

For the calculation, we consider phonon-phonon Umklapp scattering (τ_U), boundary scattering (τ_B), impurity scattering (τ_I), and normal scattering (τ_N). Therefore, per Matthiessen's rule the combined phonon relaxation time (τ_C) is,

$$\frac{1}{\tau_C} = \frac{1}{\tau_U} + \frac{1}{\tau_N} + \frac{1}{\tau_B} + \frac{1}{\tau_I} \tag{5}$$

The values of different fitting parameters used in the model are summarized in Table S1.

Table S1 Fitting parameters used in the thermal conductivity theoretical calculations for each sample: suspended length (L), Casimir length (Λ_0), longitudinal Debye temperature (θ_L), transverse Debye temperature (θ_L), longitudinal phonon group velocity (v_L), transverse phonon group velocity (v_L), longitudinal grunneiser parameter (γ_L), transverse grunneiser parameter (γ_T), phonons specularity parameter (p), mass difference scattering parameter (A).

Sample	L (μm)	Λ_0 (nm)	$\theta_L(K)$	$\theta_T(K)$	$v_L(m/s)$	$v_T(m/s)$	γ_L	γ_T	p	A (s^3)
NT1	4.29	2	855	390	8127	3715	2.4	2.2	0	$6.31\text{x}10^{-43}$
NT 2	4.21	2	855	390	8127	3715	2.4	2.2	0	$6.31\text{x}10^{-43}$
NT 3	7.85	2	855	390	8127	3715	2.4	2.2	0	$2.97\text{x}10^{-43}$
NT 4	11.94	2	855	390	8127	3715	2.4	2.2	0	$2.5\text{x}10^{-43}$

Thermoelectric modeling

The following equation presents the total Seebeck coefficient and shows both electrons and holes contributions, which correspond to two-band model Seebeck.

$$S = \frac{S_e n\mu_e + S_h p\mu_h}{n\mu_e + p\mu_h} \tag{6}$$

where n and p are the electrons and hole concentration respectively, μ_e and are μ_h electron and hole mobility. $S_{e(h)}$ are the Seebeck coefficient of electrons and holes respectively and are described by the following equations,

$$S_{e(h)} = -\frac{k_B}{e}\left(\frac{\left(r_{e(h)}+\frac{5}{2}\right)F_{r_{e(h)}+\frac{3}{2}}(\eta_{e(h)})}{\left(r_{e(h)}+\frac{3}{2}\right)F_{r_{e(h)}+\frac{1}{2}}(\eta_{e(h)})} - \eta_{e(h)}\right) \tag{7}$$

where $\eta_e = \frac{E_F}{k_B T}$ is the reduced Fermi energy for electrons and E_F is Fermi energy for the same carrier and $\eta_h = \frac{E_{Fh}}{k_B T} = -\frac{(E_F + E_g)}{k_B T}$ is the reduced Fermi energy for holes and E_{Fh} is Fermi energy for the same carrier. E_g is the bandgap, assumed to be 3.2 eV for the anatase TiO_2 and it is relatively temperature independent based on the empirical eqn (8)[2]

$$E_g(T) = E_g(0) - \frac{\alpha}{e^{(\Theta/T)} - 1} \tag{8}$$

F_t is the Fermi Dirac integral of order t and it is calculated using the following eqns:

$$F_t(\eta) = \int_0^\infty \frac{y^t dy}{e^{(y-\eta)} + 1} \tag{9}$$

In the eqn (7), k_B is the Boltzmann's constant, e is the electron charge and T is the absolute temperature.

Besides E_f, the Seebeck coefficient is assumed to be dependent on the electron/hole energy according to $\tau_{e/p} = \tau_0 E^{re/p}$ here both $r_{e/p}$ and τ_0 are two constant.[3] As reported in previous work for InSb nanowires,[4] from the extracted data of the carrier mobility, that is discussed in the main text, τ_e was found to be limited by either the boundary scattering or ionized impurity scattering in the NTs, hence $r_{e/p}$= -0.5.

The electron and hole concentrations were calculated using:

$$n = \frac{4\pi}{h^3}(2m_e^* k_B T)^{3/2} F_{\frac{1}{2}}(\eta_e) \tag{10}$$

$$p = \frac{4\pi}{h^3}(2m_h^* k_B T)^{3/2} F_{\frac{1}{2}}(\eta_h) \tag{11}$$

The previous equations describe the two-band model used to fit the measured Seebeck data and extract the E_f as a function of temperature. Thin film anatase TiO_2 data [5] is used for the carrier

effective masses, and it is expected to be close to what is in NTs. The single band model is described by eqn (7) for the n-type semiconductor and for a p-type semiconductor. Fig. S2 joins both models with the measured Seebeck. For the two-band model, we used the bulk values for electron and hole mobilities.

The determination of the E_f may be accomplished using two solutions for the two-band model and one solution for the single band model. Those solutions correspond to two different regimes, one transition regime, and another highly doped regime. Since both solutions match the measured Seebeck values, the actual value is defined by the associated electrical conductivity value.

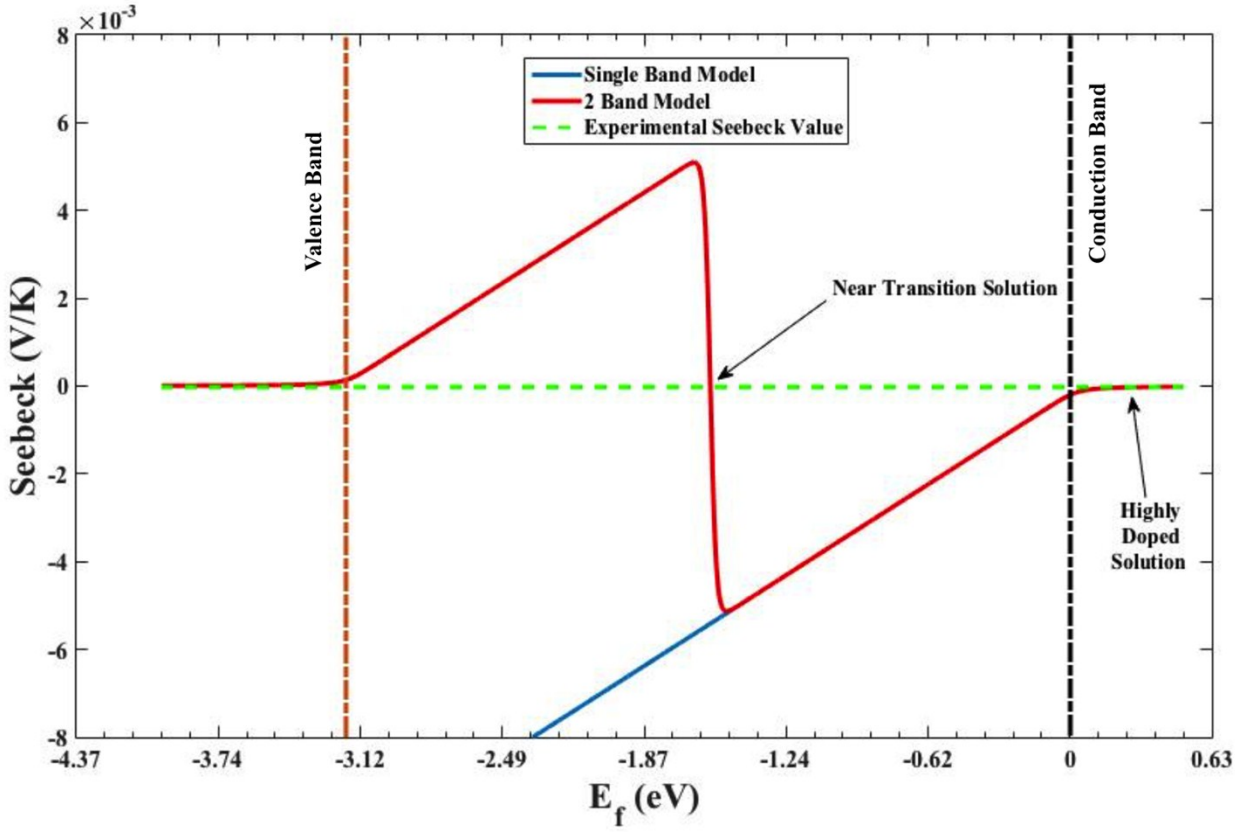

Fig. S2 Seebeck coefficient as a function of the Fermi level (E_f) for Two-band Model (red curve), Single-band Model (blue curve) and the Experimental Seebeck value (green dashed line) at T=300 K. Also shown is the conduction and valence band limit for the anatase TiO_2.

The electrical conductivity was calculated according to:

$$\sigma = ne\mu_e + pe\mu_h \tag{12}$$

Based on the two-band model, the Ef is given by the intersection of the measured Seebeck with the theoretical curve of S from eqn (6) (see Fig. S2). The first solution that associated to the near transition regime corresponds to very different electrical conductivity value compared to the actual measured value. The highly doped solution was close or superposed in both models. Fig. S3 Illustrates the position of various acceptor and donor states that facilitate the fermi level shift in the NTs 1&2 as a function of temperature.

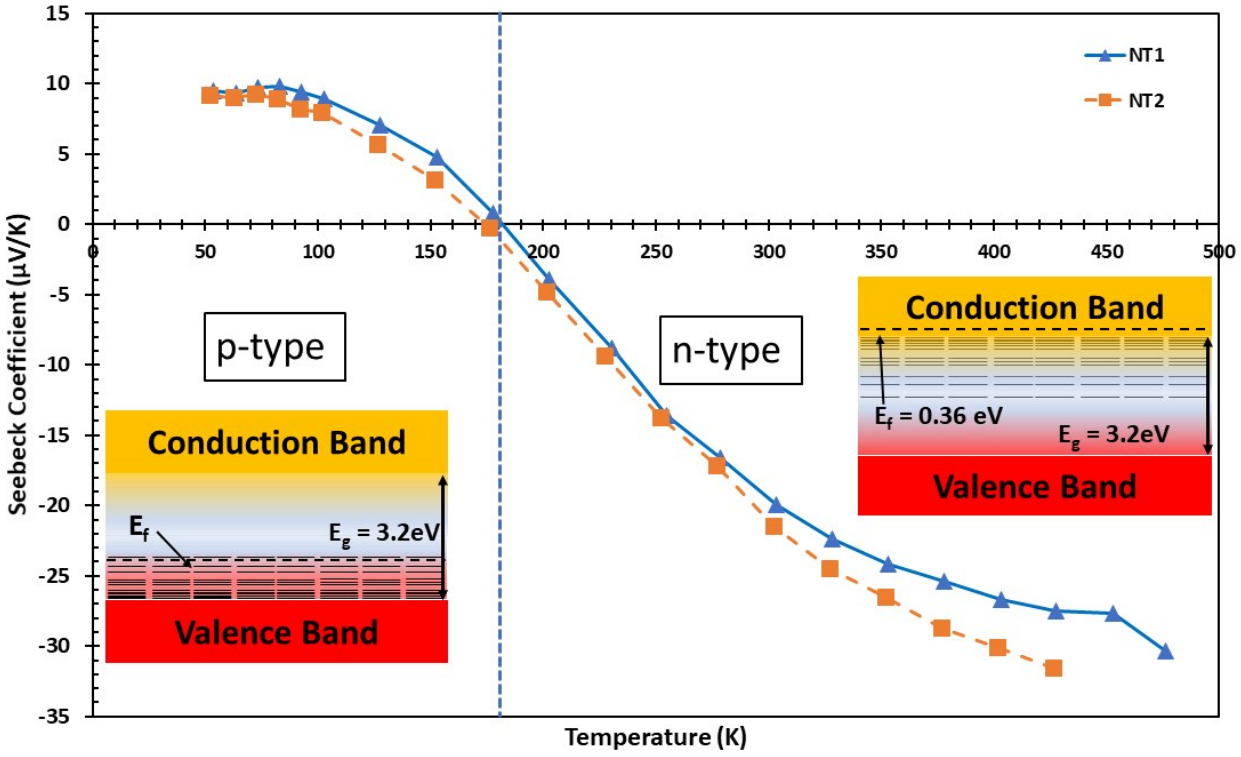

Fig. S3 Shows the temperature dependent Seebeck coefficient and corresponding energy levels at different Seebeck regime *i.e.* n-and p-type.

To further compare the fermi levels, the carrier concentration was obtained by the slope of Mott-Schottky plot Fig. S4. Measurements were performed using Na_2SO_4 (pH 8.6) in a three electrode

configuration with TiO_2 nanotube array film as the working electrode, platinum as the counter electrode and Ag/AgCl as the reference electrode at a fixed frequency of 1 kHz and in the potential range -1 V to +1 V. The NT1 film (reduced) and NT4 film (unreduced) were subjected to measurements in KOH (pH 12.8) electrolyte also to find if electrolyte pH affected the carrier concentration. The carrier concentrations and flat band potentials were calculated using the Mott-Schottky relation[6] eqn (14),

$$\frac{1}{C^2} = \frac{2}{N_D e \varepsilon \varepsilon_0 A^2}(V - V_{FB} - K_B T) \tag{13}$$

Here, e is the electronic charge, ε_0 is the permittivity of free space, N_D is donor density, V is the applied potential, V_{FB} is the flat band potential, K_B is the Boltzmann's constant, and T is the temperature. The Mott-Schottky plots for all the TiO_2 nanotube array samples are shown in the Fig. S4. The flat band potentials and doping concentrations were roughly estimated using the x-intercept and slope of the straight-line region of the plot respectively [7] and given in Table S2.

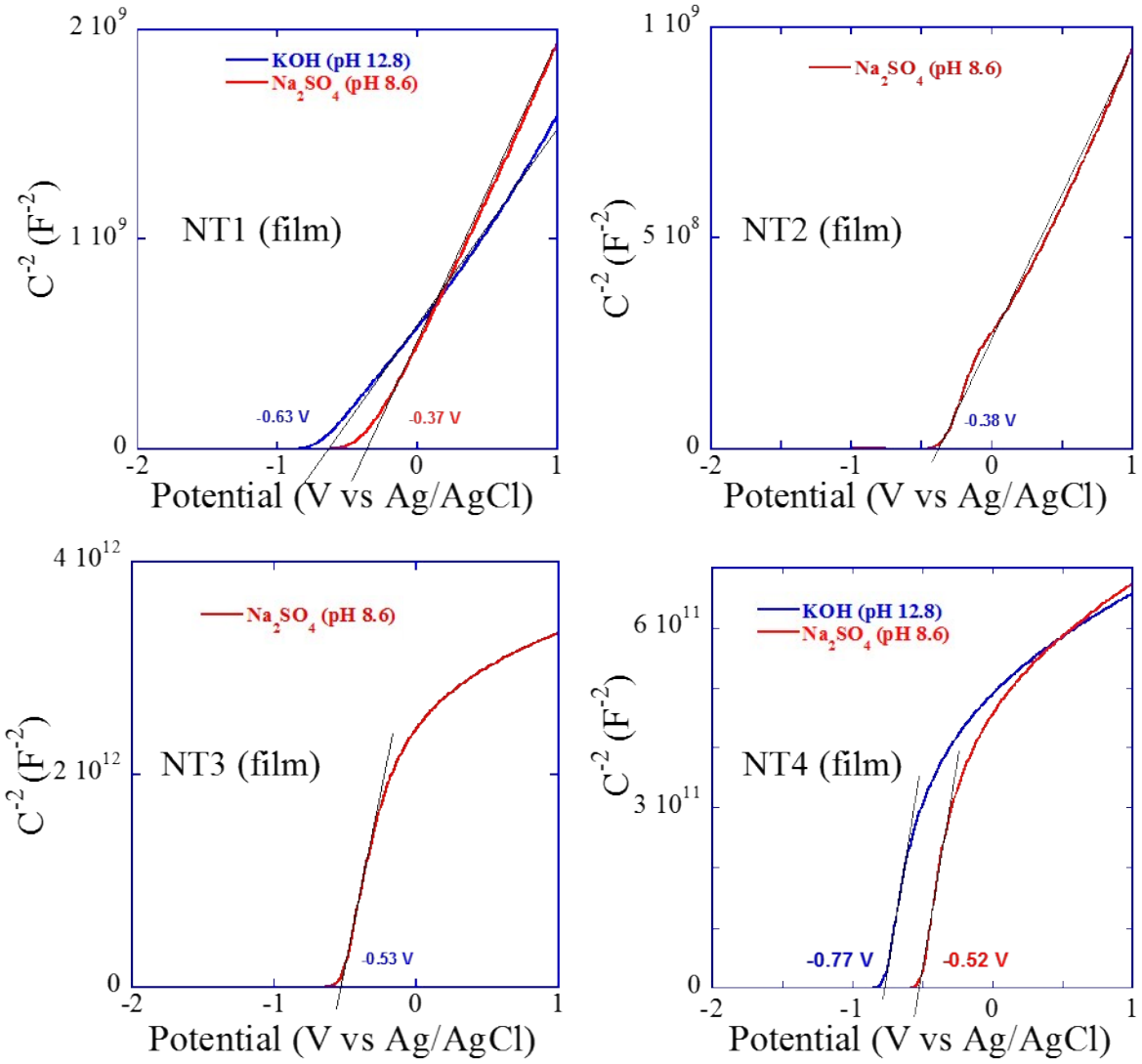

Fig. S4 Mott-Schottky plots of titania nanotube array films on titanium substrates. The flat band potentials (vs. Ag/AgCl) and electrolyte pH are shown in each graph.

Nernst relation below was used to find the flat band potentials (V_{fb}) vs NHE at pH 0 (25 °C).

$$E_{NHE} = E_{Ag/AgCl} + E^0_{Ag/AgCl} + (0.059\ pH) \qquad (14)$$

E_{NHE} and $E_{Ag/AgCl}$ are the potentials with respect to normal hydrogen electrode and Ag/AgCl respectively and $E^0_{Ag/AgCl}$ = 0.197 V vs NHE. The V_{fb} (vs NHE) are given in Table S2. It is

evident that regardless of the electrolye pH, the flat band potentials are nearly the same for weakly reduced NT3 and NT4. The V_{fb} of highly reduced samples NT1 and NT2 are also nearly the same (regardless of the electrolyte pH), but shifted slightly to the positive side. The average carrier concentration calculated from Mott-Schottky plots of different nanotube samples are also given in Table S2. Although the electron concentrations in NT1 and NT2 are nearly the same as in the case of NT3 and NT4, the reduced samples (NT1 and NT2) have the concentration four orders of magnitude higher.

Table S2 Flat band potential and electron concentration calculated from Mott-Schottky plots.

Sample	*V_{fb} (V vs NHE)*	*n (cm^{-3})*
NT1 (KOH)	*0.32*	1.6 x 10^{22}
NT1 (Na_2SO_4)	0.33	(1.9±0.7) x 10^{22}
NT2 (Na_2SO_4)	0.32	(1.5±0.2) x 10^{22}
NT3 (Na_2SO_4)	0.17	(4.4±1.0) x 10^{18}
NT4 (Na_2SO_4)	0.18	(3.0±0.6) x 10^{18}
NT4 (KOH)	0.18	5.9 x 10^{18}

The fermi level was extracted by eqn (16) and (17) respectively for non-degenerate and degenerate semiconductors. Table S3 shows the comparison between extracted and calculated positions of the Fermi levels.

$$n \cong N_c \exp\left(\frac{E_f - E_C}{kT}\right) \tag{15}$$

$$\frac{E_f - E_c}{kT} \cong \ln\left(\frac{n}{N_c}\right) + \frac{1}{\sqrt{8}}\left(\frac{n}{N_C}\right) - \left(\frac{3}{16} - \frac{\sqrt{3}}{9}\right)\left(\frac{n}{N_c}\right)^2 + \ldots \tag{16}$$

Where N_c is the intrinsic carrier concentration which is defined by

$$N_C = 2\left[\frac{2\pi\, m_e^* kT}{h^2}\right]^{3/2} \tag{17}$$

where m_e^* (effective mass of an electron) greater than 10 m_e was used for anatase TiO_2 NTs. Such large electron effective mass is due to the d-band character of the conduction band.[5] An intrinsic carrier concentration (N_C) of 8×10^{20} cm^{-3} indicate that NTs1&2 are degenerately doped and NTs 3&4 are non-degenerate. As mentioned in the main text, the difference in the E_f values for NTs can be attributed to the fact that the Mott-Schottky measurements were done on NT array samples in a liquid atmosphere, whereas the suspended microdevice measurements were done on individual nanotubes in a vacuum.

Table S3 Fermi level calculation via Mott-Schottky plots and Seebeck models.

Sample	*n* (cm^{-3})	E_f (eV) *Mott-Schottky*	E_f(eV) *Calculated*
NT1	$(1.9 \pm 0.7) \times 10^{22}$	0.37	0.35
NT2	$(1.5 \pm 0.2) \times 10^{22}$	0.29	0.37
NT3	$(4.4 \pm 1.0) \times 10^{18}$	-0.13	0.06
NT4	$(3.0 \pm 0.6) \times 10^{18}$	-0.14	0.08

The activation energy for NT1&2 were calculated using the temperature dependent mobility data for the respective nanotubes. Fig. S5 shows the activation energy for NT1 &2 to be 32 meV, which can be considered shallow and thermally activated.

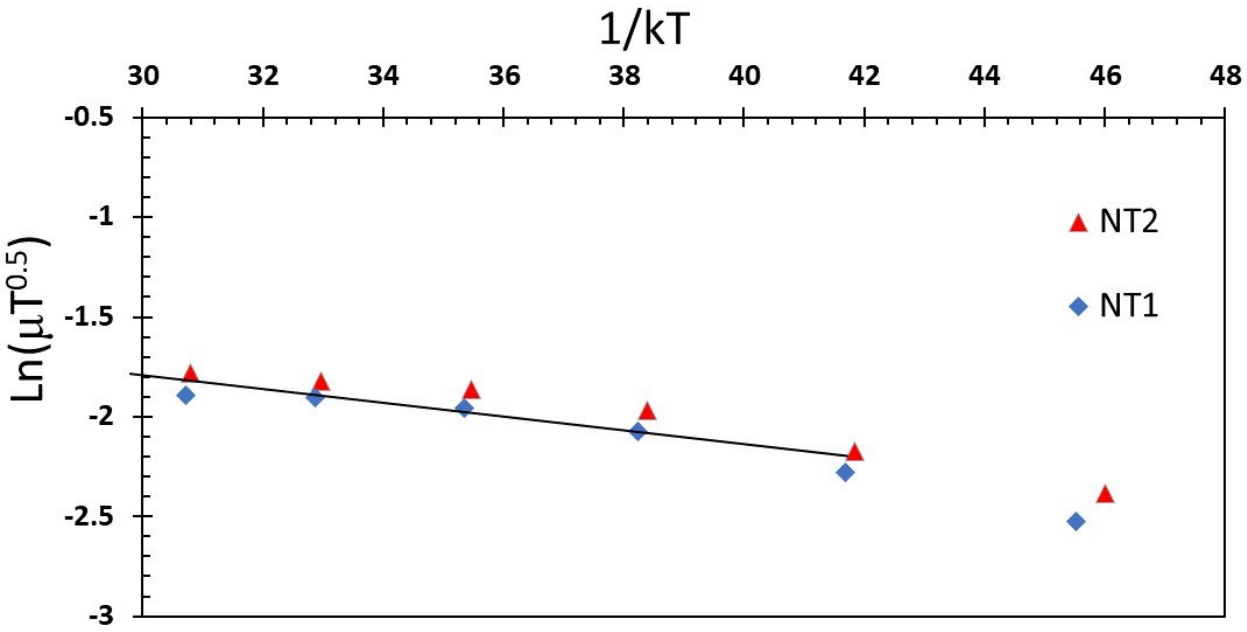

Fig. S5 Plots the logarithm of $\mu_{eff} = \mu_o \left(\frac{1}{T}\right)^{\frac{1}{2}} \exp\left(\frac{-E_a}{kT}\right)$ [8,9] and fitting the high temperature data gives activation energy of 32 meV for NT1&2.

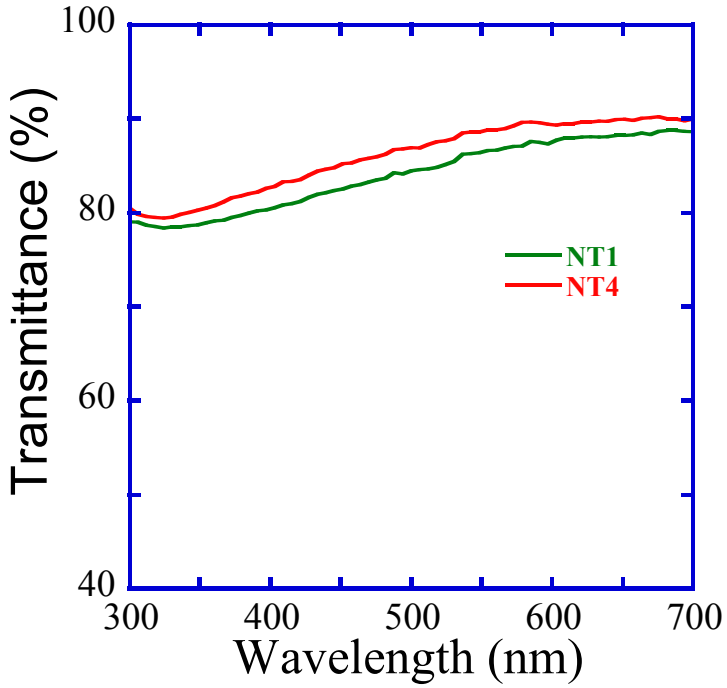

Fig. S6. Transmittance spectra of nanotubes NT1 and NT4 dispersed in water at very low concentrations.

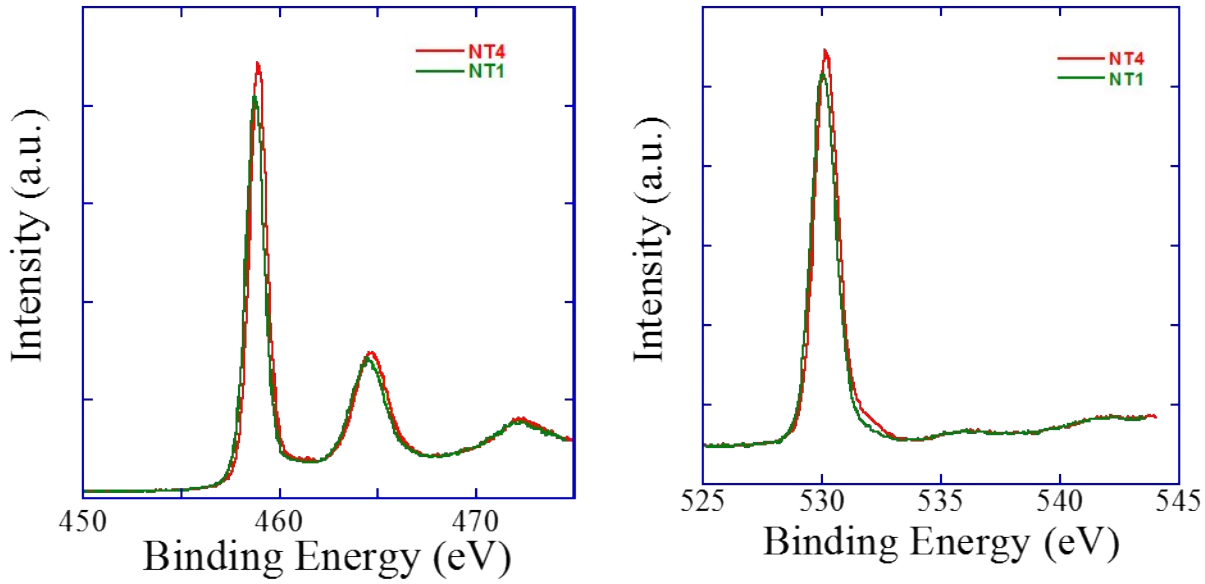

Fig. S7. X-ray photoelectron spectra of NT1 and NT4 showing the Ti 2*p* (left) and Ti O1*s* (right) peaks.

Notes and references

1 D. T. Morelli, J. P. Heremans and G. A. Slack, *Phys. Rev. B*, 2002, **66,** 195304.

2 F. Zhang, R. J. Zhang, D. X. Zhang, Z. Y. Wang, J. P. Xu, Y. X. Zheng, L. Y. Chen, R. Z. Huang, Y. Sun, X. Chen, X. J. Meng and N. Dai, *Appl. Phys. Express*, 2013, **6,** 121101.

3 A. Mavrokefalos, A. L. Moore, M. T. Pettes, L. Shi, W. Wang and X. Li, *J. Appl. Phys.*, 2009, ***15*,** 104318.

4 J. H. Seol, A. L. Moore, S. K. Saha, F. Zhou and L. Shi, *J. Appl. Phys.*, 2007, **101,** 023706.

5 B. Enright and D. Fitzmaurice, *J. Phys. Chem.*, 1996, **100,** 1027-1035.

6 F. Cardon and W. P. Gomes, *J. Phys. D: Appl. Phys.*, 1978, **11,** 63-67.

7 F. Fabregat-Santiago, G. Garcia-Belmonte, J. Bisquert, P. Bogdanoff and A. Zaban, *J. Electrochem. Soc*., 2003, **150,** 293-298.

8 J.Y.W. Seto, J.Appl.Phys.,1975, **46**, 5247.

9 J. Martin, L. Wang, L. Chen and G. S. Nolas, Physical Review B, 2009, **79**, 115311.